Article | Open Access

Energy Materials

Qin *et al. Energy Mater.* **2026**, *6*, 600104 **DOI:**10.20517/energymater.2026.150

A ferrocyanide-polysulfide redox flow battery with homogeneous catalysis for high-performance energy storage

Chao Qin[1,2], Xi Xu[1,2], Zhizhao Xu[3], Chunhui Gao[2], Bo Lu[4], Mei Ding[2], Chuankun Jia[1,2,*]

Keywords:
Ferrocyanide-polysulfide redox flow battery, neutral supporting electrolyte, homogeneous catalysis, long-term cycling stability, high-rate performance

Citation: Qin, C.; Xu, X.; Xu, Z.; Gao, C.; Lu, B.; Ding, M.; Jia, C. A ferrocyanide-polysulfide redox flow battery with homogeneous catalysis for high-performance energy storage. *Energy Mater.* **2026**, *6*, 600104. https://dx.doi.org/10.20517/energymater.2026.150

Received: 3 Jun 2026
First Decision: 29 Jun 2026
Revised: 24 Jul 2026
Accepted: 20 Aug 2026
Published: 25 Aug 2026

Academic Editor:
Yuping Wu
Copy Editor:
Shu-Yuan Duan
Production Editor:
Shu-Yuan Duan

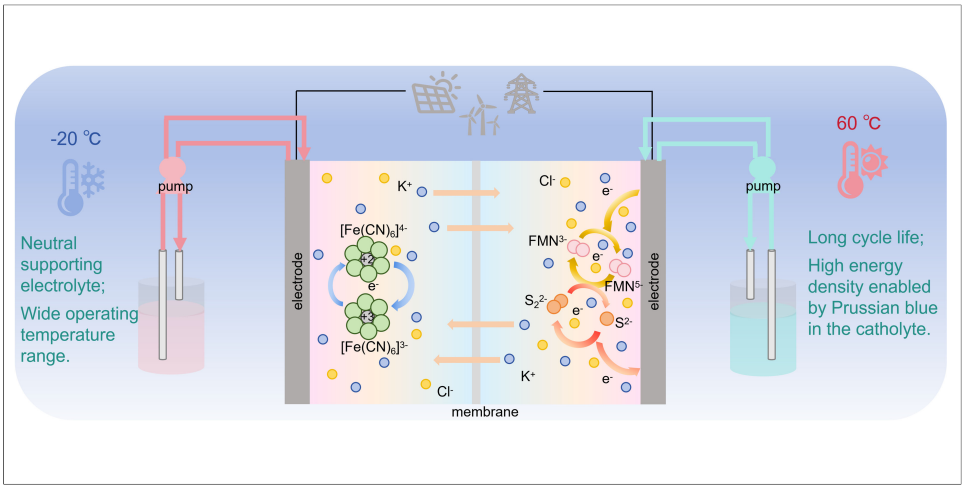

Abstract

Aqueous ferrocyanide-polysulfide redox flow batteries (Fe-S RFBs) are promising for grid-scale energy storage yet suffer from slow polysulfide kinetics, membrane crossover, and supporting-electrolyte mismatch, which increase polarization and undermine cycling durability. Although riboflavin sodium phosphate (FMN-Na) has been used as a homogeneous catalyst to promote polysulfide conversion, previous formulations relied on externally added KOH, creating an OH^-/Cl^- imbalance and placing greater demands on membrane selectivity. Herein, we construct a KOH-free Fe-S RFB using KCl as the common supporting electrolyte and FMN-Na as a homogeneous molecular catalyst. The system utilizes the alkalinity generated by K_2S hydrolysis, removing the need for added KOH while providing a suitable pH environment for FMN-Na electrocatalysis. Whereas earlier work focused on long-chain polysulfide reduction, FMN-Na facilitates polysulfide conversion dominated by the S_2^{2-}/S^{2-} couple through electron shuttling, reducing polarization and

[1]College of Materials Science and Engineering, Changsha University of Science & Technology, Changsha 410114, Hunan, China.
[2]Institute of Energy Storage Technology, College of Energy and Power Engineering, Changsha University of Science & Technology, Changsha 410114, Hunan, China.
[3]School of Transportation, Changsha University of Science & Technology, Changsha 410114, Hunan, China.
[4]School of Light Industry and Engineering, State Key Laboratory of Advanced Papermaking and Paper-based Materials, South China University of Technology, Guangzhou 510641, China

***Correspondence to:** Prof. Chuankun Jia, College of Materials Science and Engineering, Changsha University of Science & Technology, Changsha 410114, Hunan, China; Institute of Energy Storage Technology, College of Energy and Power Engineering, Changsha University of Science & Technology, Changsha 410114, Hunan, China. E-mail: jiachuankun@csust.edu.cn

improving reversibility. The optimized Fe-S RFB delivers outstanding cyclability with 5,000 stable cycles at 40 mA cm^{-2} and a peak power density of 197.2 mW cm^{-2}. With a high-concentration catholyte, the cell yields an initial energy efficiency (EE) of 83.07% and retains 77.34% after 440 cycles. Tailoring the electrolyte compositions extends operation from -20 to 60 °C. Furthermore, Prussian blue-mediated redox targeting and increased active-material concentrations yield a catholyte-volume-normalized discharge energy density of 102.12 Wh L^{-1}, corresponding to 51.06 Wh L^{-1} when normalized to the combined electrolyte volume. This work provides a practical route towards low-cost Fe-S RFBs combining durable cycling, wide-temperature operation, and high electrolyte-level energy density for grid-scale storage.

INTRODUCTION

Global energy demand is still predominantly satisfied by fossil fuels. Their gradual depletion, coupled with climate change induced by CO_2 emissions, has spurred the exploration of green renewable energy sources[1-6]. Given the swift expansion of wind and solar energy, their intrinsic instability and intermittency result in "energy curtailment" during large-scale grid integration[7-9]. Therefore, energy storage systems must be inherently safe, affordable, and scalable to achieve stable grid integration[10-13]. Pumped hydro storage, while mature, is geographically constrained, and lithium-ion batteries suffer from safety concerns such as fire and explosion risks[14-16]. Aqueous redox flow batteries (ARFBs) stand out as one of the most competitive candidates owing to their decoupled power and energy configuration, high safety, deep-discharge capability, and flexible design[17-22]. Among various ARFBs, all-vanadium systems have been extensively investigated and commercially demonstrated, yet they still suffer from the high cost and limited reserves of vanadium, as well as its low solubility in electrolyte[23-27]. Additionally, the strong corrosivity of acidic electrolyte imposes stringent requirements on corrosion-resistant hardware, further increasing costs[28,29]. These challenges drive the exploration of next-generation ARFBs based on earth-abundant elements and environmentally benign electrolytes.

Ferrocyanide-polysulfide redox flow batteries (Fe-S RFBs), which employ polysulfide species and the ferricyanide/ferrocyanide ($[Fe(CN)_6]^{3-/4-}$) redox couple as active materials, represent such an attractive system [30,31]. Iron and sulfur are abundant in the Earth's crust and inexpensive, giving the Fe-S RFB system the potential for low cost. Typically, the $[Fe(CN)_6]^{3-/4-}$ pair exhibits fast kinetics and excellent stability in neutral or weakly alkaline electrolyte, while polysulfide electrolytes provide high theoretical capacity and low material cost. Furthermore, the solubility of $[Fe(CN)_6]^{4-}$ in the electrolyte is markedly enhanced to 1.6 M via the hetero-ionic effect, which helps improve the energy density of the battery[32]. However, the practical performance of Fe-S RFBs is severely limited by the negative-side polysulfide electrolyte. Dissolving commercial K_2S with a purity of ≥ 40% results in a complex mixture of various polysulfide species (denoted as S_x^{2-}, where x = 1, 2, 4, 6, *etc.*), leading to multiple, overlapping redox processes. Furthermore, polysulfide interconversion is intrinsically sluggish[33-35]. Polysulfide species are also prone to membrane crossover, resulting in active-material loss, sulfur deposition, electrolyte cross-contamination, and capacity decay[30-31]. Together, these kinetic and transport limitations increase cell polarization, restrict the operating current density, and compromise the energy efficiency (EE) and cycling stability of Fe-S RFBs[30,31,35].

To overcome polysulfide-related kinetic barriers, considerable attention has focused on electrode modification with heterogeneous catalysts (e.g., metal sulfides, carbon-based composites)[36,37]. Although such strategies improve electrochemical activity to a certain extent, they involve complex preparation processes and offer limited active sites, which restrict rate capability and long-term durability. Alternatively, the single-molecule redox-targeting (SMRT) concept has been employed to enhance RFB energy density[38]. Parallel to these strategies, a homogeneous molecular catalysis strategy has been explored to accelerate polysulfide conversion by using soluble redox mediators to transfer electrons in the bulk electrolyte[39]. For instance,

flavin mononucleotide sodium salt (FMN-Na) dissolved in the electrolyte was reported to catalytically enhance the reduction of S_4^{2-} to S_2^{2-}, transforming a slow electrochemical step into a faster chemical process[40]. However, previous demonstrations mainly focused on catalyzing the reduction of long-chain polysulfide (S_4^{2-}) in a strongly alkaline anolyte containing KOH, while the ferrocyanide ($[Fe(CN)_6]^{4-}$) catholyte used KCl as the supporting electrolyte. Studies of pH-decoupled aqueous flow batteries have shown that pH gradients can drive acid-base crossover and electrolyte pH drift, thereby penalizing EE and cycling stability[30,41]. Hydroxide-ion migration and changes in electrolyte pH during operation have also been observed in Fe-S RFB cells[30]. In addition, strongly alkaline conditions may compromise the long-term stability of Ferri/ferrocyanide electrolytes[42].

In this work, we develop a KOH-free, homogeneously catalyzed Fe-S RFB by employing KCl as the common supporting electrolyte in both half-cells and FMN-Na as an active and durable molecular catalyst [Scheme 1]. This electrolyte design avoids externally added KOH and reduces the pH and supporting-anion disparity between the two half-cells. Ultraviolet-visible (UV-vis) spectroscopy coupled with electrochemical analysis indicates that the sulfur species in our K_2S-KCl electrolyte primarily exists as $S_{\sim1.7}^{2-}$, which we approximate as S_2^{2-}. Although polysulfide solutions contain a distribution of species, their redox potentials are sufficiently distinct, allowing a dominant pair to govern the electrochemical response. Differing from earlier work targeting S_4^{2-}/S_2^{2-}conversion, this catalyst specifically promotes the reversible redox of S_2^{2-}/S^{2-}, the dominant reaction in the proposed cell. The self-generated alkalinity from sulfide hydrolysis provides a suitable environment for FMN-Na catalysis without additional alkali. Systematic electrochemical and spectroscopic characterizations reveal that FMN-Na effectively mediates electron transfer and boosts the polysulfide reduction kinetics. As a result, the assembled Fe-S RFB exhibits significantly reduced polarization, enhanced EE, and superior cycling stability. Beyond stable cycling, we further pushed the operating temperature limits to -20 °C and 60 °C by simply adjusting the electrolyte composition. Moreover, by elevating active-material concentrations and integrating Prussian blue-mediated redox targeting, the total-electrolyte-volume-normalized discharge energy density reaches a record value of 51.06 Wh L^{-1}. Even with a high-concentration catholyte, the cell delivers an initial EE of 83.07% and retains an EE of 77.34% at the end of the 440th cycle. This study establishes a high-performance, KOH-free Fe-S RFB and provides a practical approach to coupling self-generated alkalinity with homogeneous molecular catalysis for low-cost, long-duration aqueous energy storage.

EXPERIMENTAL

Materials and methods

All chemicals were used without further purification unless otherwise specified. Potassium sulfide (≥ 40% K_2S), potassium chloride (KCl, 99.5%), potassium ferrocyanide ($K_4[Fe(CN)_6]\cdot3H_2O$, 99.5%), sodium ferrocyanide ($Na_4[Fe(CN)_6]\cdot3H_2O$, 99.5%), potassium hydroxide (KOH, 99.5%), potassium acetate (KAc, 99.0%), urea (CH_4N_2O, 99.5%), and Prussian blue (PB) were bought from Sinopharm Chemical Reagent Co., Ltd. Riboflavin sodium phosphate (FMN-Na, 93.0%) was ordered from Shanghai Aladdin Biochemical Technology Co., Ltd. Perfluorosulfonic acid (PFSA) ion-exchange membrane (IEM) was supplied by Dongyue Group.

Pretreatment of membrane

In this work, a K^+-type IEM was necessary. Therefore, the purchased H^+-type IEM needed to be treated to convert it into a K^+-type IEM. The H^+-type membrane was cut into pieces, immersed in a 1.0 M KOH solution, and heated at 80 ℃ for 1.5 h. Subsequently, the membrane pieces were rinsed thoroughly with deionized water to yield the desired K^+-type membranes.

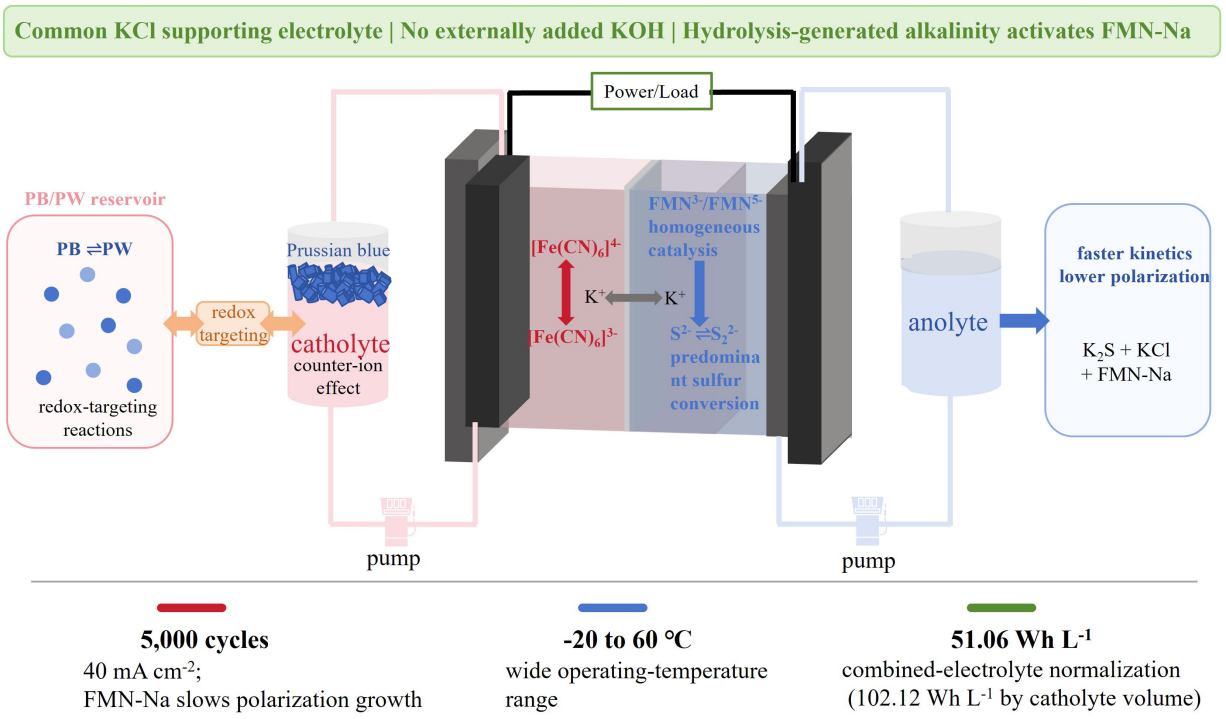

Scheme 1. Overall schematic of the KOH-free Fe-S RFB, illustrating FMN-Na-mediated polysulfide conversion and PB/Prussian White (PW) redox targeting in the catholyte. FMN-Na: Flavin mononucleotide sodium salt; RFB: redox flow battery.

Preparation of K_2S electrolyte

To prepare K_2S electrolytes at the desired concentrations, calculated amounts of solid K_2S and KCl were weighed and transferred into a beaker containing deionized water as the solvent. The mixture was manually stirred with a glass rod at room temperature (~ 25 ℃) until both solids were fully dissolved. The solution was then left undisturbed for 2 h to obtain a clear and homogeneous electrolyte. For electrolytes containing the catalyst, 30.0 mM FMN-Na was added to the as-prepared K_2S electrolyte and dissolved completely before use.

Electrochemical measurements

Electrochemical performance testing was conducted using an electrochemical workstation from Bio-Logic (VSP 150, France). Cyclic voltammetry (CV) measurements were conducted in a standard three-electrode configuration, where a glassy carbon electrode served as the working electrode, a Hg/Hg_2Cl_2 electrode as the reference electrode, and a Pt mesh as the counter electrode. 50.0 mM K_2S in 1.0 M KCl was employed as the electrolyte. The pH values of the electrolytes were measured using a Leici laboratory pH meter (PHSJ-3F, Shanghai, China). The UV-Vis absorption spectra were measured using a Varian ultraviolet-visible spectrophotometer (Cary 500 UV-Vis-NIR, USA). For anolyte samples collected at different SOCs after the same number of cycles, a 10,000-fold dilution was required before spectroscopic testing. The Fe-S RFB cells were assembled with a K^+-type IEM as the separator, and carbon felt served as the electrodes. Electrochemical tests were carried out on a Neware battery test system (CT-4008 T-5V 6A-S1, Shenzhen, China). For the galvanostatic intermittent titration technique (GITT) tests, a current density of 10 mA cm^{-2} was applied, and a relaxation time of 30 s at open circuit was allowed. Rate performance was evaluated by recording the CE and EE values over eight charge-discharge cycles at each current density. The polarization curve was obtained using the Arbin battery testing system (BT-I, USA). The testing procedure started with a discharge at 140 mA, followed by a linear increase of the discharge current to 10 A at 10 mA s^{-1}, stopping early if the voltage reached 0 V. Separate long-term cycling tests were run under galvanostatic conditions at

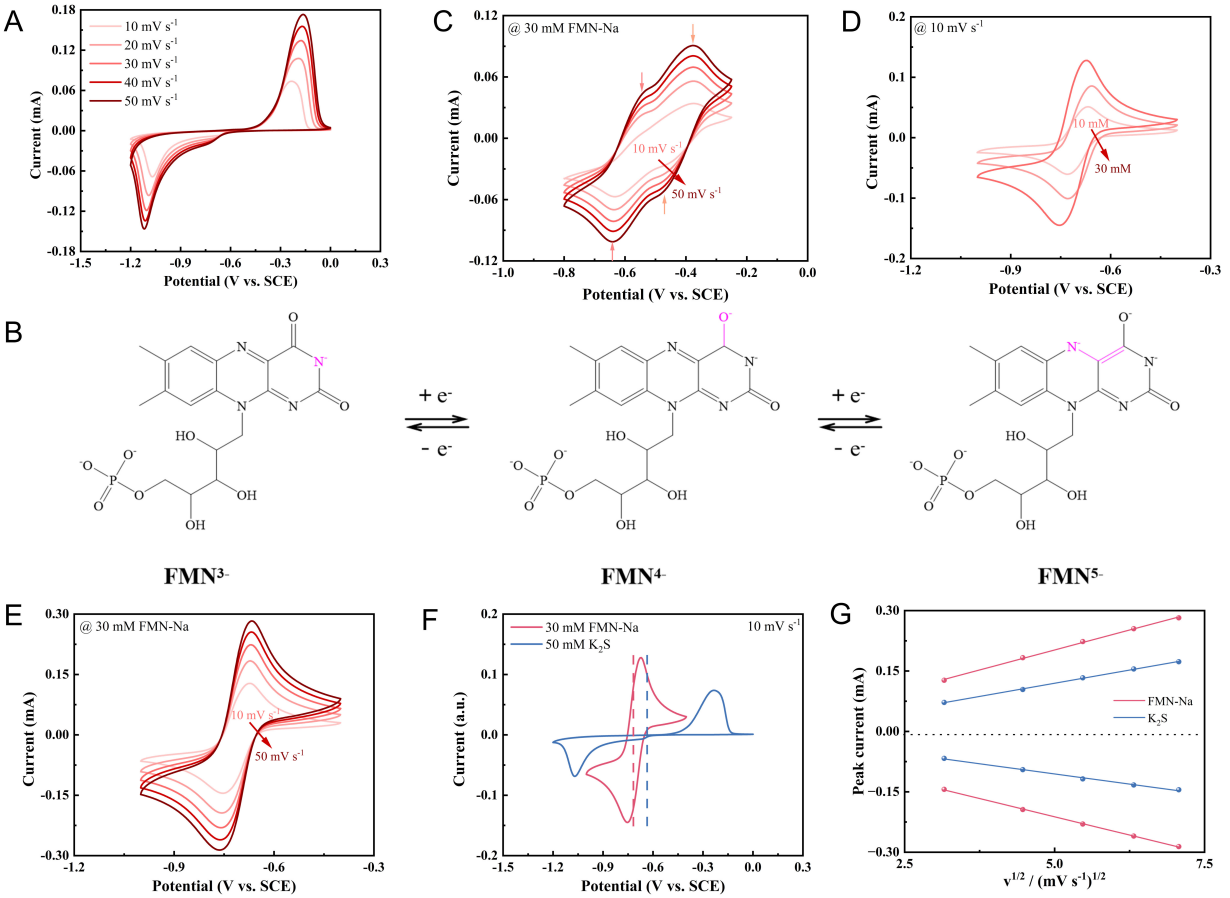

Figure 1. (A) Cyclic voltammograms of K_2S in KCl electrolyte at different scan rates; (B) Schematic representation of the redox reaction of FMN-Na; (C) Cyclic voltammograms of FMN-Na in KCl electrolyte at scan rates ranging from 10 to 50 mV s^{-1}; (D) Cyclic voltammograms of FMN-Na in alkaline electrolyte at different concentrations, recorded at 10 mV s^{-1}; (E) Cyclic voltammograms of 30.0 mM FMN-Na in alkaline electrolyte at varying scan rates; (F) Comparison of cyclic voltammograms for K_2S in KCl electrolyte and FMN-Na in alkaline electrolyte, both recorded at 10 mV s^{-1}; (G) Plots of redox peak currents against the square root of scan rate for the S_2^{2-}/S^{2-} redox pair and the FMN^{3-}/FMN^{5-} couple. FMN-Na: Flavin mononucleotide sodium salt; SCE: saturated calomel electrode.

40 mA cm^{-2}, within a voltage range of 0.4-1.4 V. To evaluate the performance of the Fe-S RFB with high-concentration electrolytes, the same cell was first subjected to four charge-discharge cycles without PB, during which the EE and discharge capacity reached stable values. At the beginning of the fifth charging step, PB was immediately added to the catholyte, and cycling was continued under otherwise identical conditions to allow a direct comparison of the cell performance before and after PB addition. The volumetric energy density was calculated by dividing the total discharge energy by the volume of the capacity-limiting catholyte.

RESULTS AND DISCUSSION

A K_2S solution was prepared with KCl as the supporting electrolyte, and cyclic voltammetry measurements were conducted at various scan rates. A pair of distinct redox peaks was observed in the CV profile [Figure 1A]. Owing to the limited purity of commercial K_2S (≥ 40%), multiple polysulfide species S_x^{2-} (mainly x = 1, 2, 4, and 6) coexist in the as-prepared solution. Combining electrochemical capacity calculation and the state-of-charge-dependent UV-vis spectral changes, and comparison with reported aqueous polysulfide electrochemistry, the S_2^{2-}/S^{2-} couple is assigned as the predominant electrochemically active couple in the K_2S-derived electrolyte prepared without added elemental sulfur. The redox peak at -0.40 V (*vs.* SHE) is therefore mainly assigned to the conversion between S^{2-} and S_2^{2-} [Equation 1]. As the scan rate increases, the peak potential separation gradually widens, and the peak current rises. Based on the peak potential separation (E_0) and the ratio of anodic to cathodic peak currents (i_{pa}/i_{pc}) [Supplementary Table 1], the electrochemical reaction in the K_2S solution exhibits poor reversibility, confirming the need for a molecular catalyst.

$$S_2^{2-} + 2e^- \rightarrow 2S^{2-} \quad (1)$$

Such a catalyst can transform the sluggish, poorly reversible heterogeneous electron transfer between polysulfides and the electrode into a fast, homogeneous chemical redox process in the bulk electrolyte. To achieve this catalytic mechanism, the catalyst's redox potential must be more negative than that of the polysulfide species, enabling efficient reduction of S_2^{2-} or S_4^{2-} ions during charging. As previously reported, FMN-Na undergoes a typical two-electron redox reaction [Figure 1B]. In neutral KCl electrolyte, FMN-Na shows two pairs of redox peaks in its CV profile, indicating a stepwise two-electron transfer [Figure 1C, Supplementary Table 2 and Equations 2 and 3]. This stepwise behavior is also evident in cyclic voltammograms recorded at various scan rates in 10.0 mM and 20.0 mM FMN-Na [Supplementary Figure 1]. The corresponding redox potentials are -0.18 V and -0.35 V (*vs.* SHE), respectively. These potentials are more positive than those of S_2^{2-}/S^{2-} [-0.40 V *vs.* standard hydrogen electrode (SHE)] and thus cannot effectively catalyze the reduction of S_2^{2-} or S_4^{2-} to S^{2-}.

$$FMN^{3-} + e^- \rightarrow FMN^{4-} \quad (2)$$

$$FMN^{4-} + e^- \rightarrow FMN^{5-} \quad (3)$$

Given that the K_2S-KCl solution becomes alkaline (pH = 12.3) due to S^{2-} hydrolysis, the pH of the solution decreases to 11.30 after adding 30 mM FMN-Na [Supplementary Figure 2]. For the CV measurements, the pH of the FMN-Na electrolyte was therefore adjusted to 11.30 with KOH to reproduce this pH condition. Under such alkaline conditions, FMN-Na exhibits a pair of highly reversible redox peaks with a formal potential at -0.48 V (*vs.* SHE) [Figure 1D]. The maximum stable concentration of FMN-Na in this alkaline electrolyte is 30.0 mM. Further increases in the concentration cause turbidity [Supplementary Figure 3]. CV tests at various scan rates using 30.0 mM FMN-Na in alkaline medium show that the peak current increases continuously with scan rate while the peak potential remains nearly unchanged, demonstrating high reversibility and stability [Figure 1E and Supplementary Table 3]. Under these conditions, the more negative redox potential of FMN-Na enables reduced FMN-Na to mediate the reduction of oxidized polysulfide species, causing a net conversion toward S^{2-}, although S_2^{2-}, S_4^{2-}, and other polysulfide species may coexist in dynamic equilibrium. Because S_2^{2-} is the predominant oxidized polysulfide species in this electrolyte, the S_2^{2-}/S^{2-} couple is used here to represent the broader polysulfide conversion [Figure 1F and Equations 4 and 5].

$$FMN^{3-} + 2e^- \rightarrow FMN^{5-} \quad (4)$$

$$FMN^{5-} + S_2^{2-} \rightarrow FMN^{3-} + 2S^{2-} \quad (5)$$

Furthermore, the peak currents of both the $FMN^{3-/5-}$ and S_2^{2-}/S^{2-} redox couples exhibit a linear relationship with the square root of the scan rate [Figure 1G], indicating a substantial contribution from diffusion-related mass transport. The apparent diffusion coefficients (D_{app}) were estimated using the Randles-Sevcik equation [Equation 6],

$$I_p = 2.69 \times 10^5 \times n^{3/2} \times A \times C \times D_{app}^{1/2} \times v^{1/2} \quad (6)$$

where I_p, n, A, C, D_{app}, and v denote the peak current (A), number of electrons transferred, electrode area (cm^2), concentration of the electroactive species (mol cm^{-3}), apparent diffusion coefficient (cm^2 s^{-1}), and scan rate (V s^{-1}), respectively. The estimated D_{app} values for the anodic and cathodic processes of the $FMN^{3-/5-}$ couple were 6.04×10^{-7} and 5.05×10^{-7} cm^2 s^{-1}, respectively. The corresponding values for the polysulfide

redox processes were 8.05 × 10^{-8} and 5.62 × 10^{-8} cm^2 s^{-1}. However, because the latter involve coupled electron-transfer and chemical reactions, as well as interconversion among multiple polysulfide species, these values represent combined transport-kinetic parameters rather than intrinsic diffusion coefficients. They are therefore used only for comparison under the same experimental conditions.

Based on these findings, we designed an Fe-S RFB using FMN-Na as a homogeneous molecular catalyst in the anolyte [Figure 2A]. Unlike previously reported systems that use different supporting electrolytes for the catholyte and anolyte (i.e., KCl for one side and KOH for the other), both half-cells in our system employ neutral KCl as the supporting electrolyte. The anolyte becomes alkaline through spontaneous hydrolysis of sulfide ions, creating an in situ alkaline environment that enables efficient catalytic activity of FMN-Na. First, for the Fe-S RFB without FMN-Na, we selected five typical states of charge (SOCs) from 0% to 100%. Anolyte samples were diluted and analyzed by UV-vis absorption spectroscopy. The results show that during charging, the S^{2-} content gradually increases while the S_2^{2-} and S_4^{2-} contents continuously decrease [Figure 2B]. This trend confirms that the electrochemical reaction in the anolyte is dominated by the conversion of S_2^{2-} to S^{2-}, consistent with the proposed mechanism. For comparison, we collected anolyte samples at the same SOC from the Fe-S RFB with FMN-Na and performed the same UV-vis measurements. The evolution trend of polysulfide species is similar to that of the battery without FMN-Na. The S^{2-} concentration rises gradually, while S_2^{2-} and S_4^{2-} contents at the same SOC decline during charging [Figure 2C]. At the same SOC, the FMN-Na-containing anolyte exhibits a faster relative increase in the absorbance assigned to S^{2-} and lower normalized residual absorbance values assigned to S_2^{2-} and S_4^{2-} than the catalyst-free anolyte [Figure 2D], indicating accelerated polysulfide conversion during charging. Although the polysulfide electrolyte contains a minor proportion of S_4^{2-}, the overall redox behavior is dominated by the S_2^{2-}/S^{2-} conversion. FMN-Na serves as an efficient molecular accelerator to boost the sluggish kinetics of this major redox couple. Meanwhile, FMN-Na enables the kinetic reduction of inert S_4^{2-} into S_2^{2-}, which is further transformed into S^{2-}, thus enriching the population of electrochemically active sulfur species in the electrolyte. These results reveal that the overall electrochemical reactions are governed by the interconversion of short-chain disulfide species coupled with the electron-shuttling catalytic pathway mediated by FMN-Na.

We then performed polarization tests on Fe-S RFBs without and with FMN-Na in the anolyte [Figure 3A and B]. At different SOC levels, the cell with FMN-Na shows a higher peak power density than the one without the catalyst [Figure 3C]. Specifically, at 100% SOC, the peak power density reaches 197.2 mW cm^{-2} with FMN-Na, which is 11% higher than that without the catalyst (178.1 mW cm^{-2} at 100% SOC). Thus, adding FMN-Na to the anolyte effectively promotes polysulfide redox kinetics, reduces cell polarization, and improves peak power density.

Galvanostatic intermittent titration technique (GITT) curves further support this conclusion. The deviation from the equilibrium potential is 32.0 mV for the cell with FMN-Na, lower than the 37.8 mV observed without FMN-Na [Figure 3D]. Next, we compared rate performance at current densities from 20 to 100 mA cm^{-2} in 20 mA cm-2 steps [Figure 3E]. The EE of the FMN-Na cell is higher than that of the catalyst-free cell at all five current densities, and this advantage becomes more pronounced at higher current densities [Figure 3F]. This is because polarization increases with current density due to internal resistance, but the FMN-Na cell consistently maintains lower polarization. When the current density returns to the initial 20 mA cm^{-2}, the EE values of both cells recover to their initial levels, indicating good stability. Voltage-capacity curves at 40 and 100 mA cm^{-2} also confirm that the FMN-Na cell exhibits smaller polarization [Figure 3G and H].

The FMN-Na catalyst significantly improves the long-term cycling performance of the Fe-S RFB. As shown in Figure 4A, the CE remains high and stable throughout cycling regardless of the presence of FMN-Na, indicating that the active materials are stable. The average CE over the entire cycle life is 99.83% with

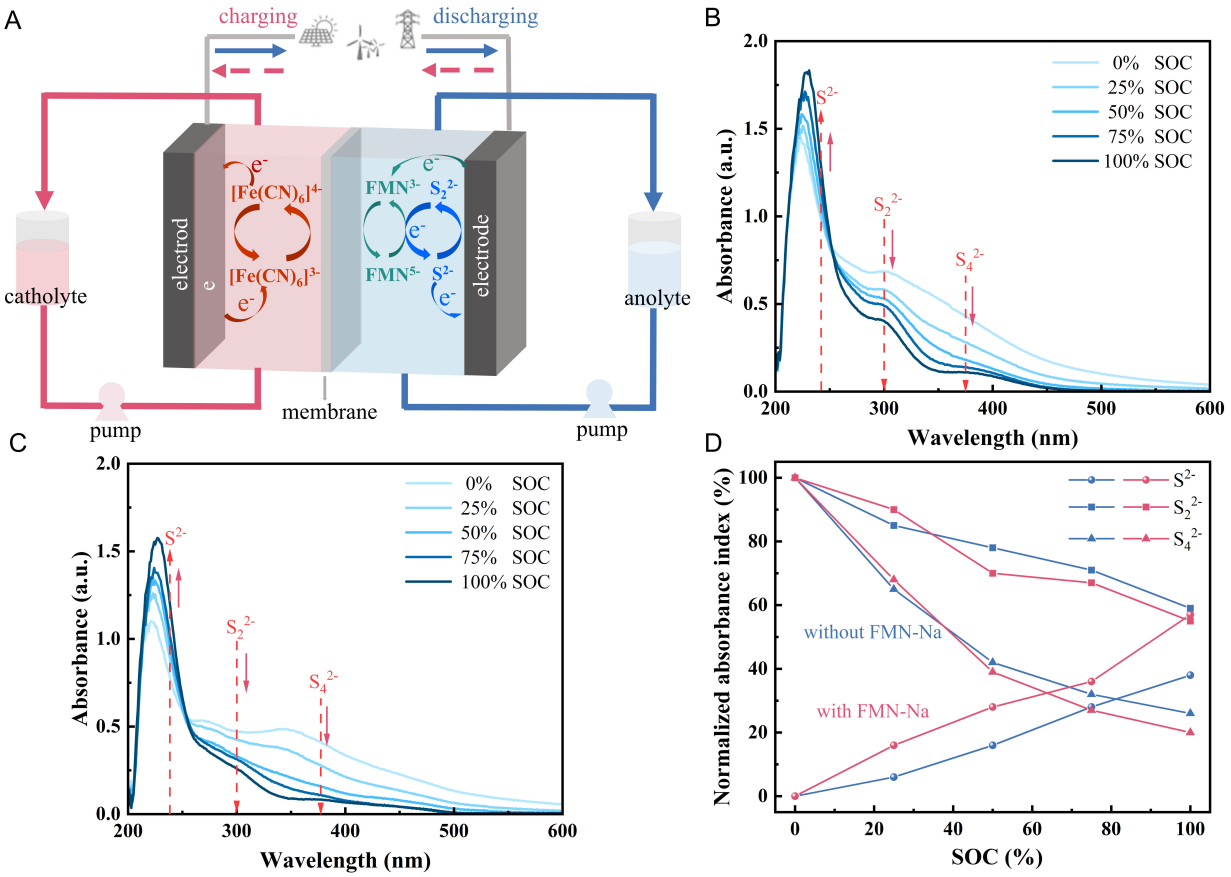

Figure 2. (A) Schematic illustration of homogeneous FMN-Na catalysis in a ferrocyanide-polysulfide redox flow battery (Fe-S RFB) with KOH-free supporting electrolyte; (B and C) Ultraviolet-visible (UV-vis) spectra of diluted anolytes collected at different SOCs (B) without and (C) with 30.0 mM FMN-Na. (D) SOC-dependent normalized absorbance indices of sulfur species in the anolytes with and without 30.0 mM FMN-Na. FMN-Na: Flavin mononucleotide sodium salt; SOC: state of charge.

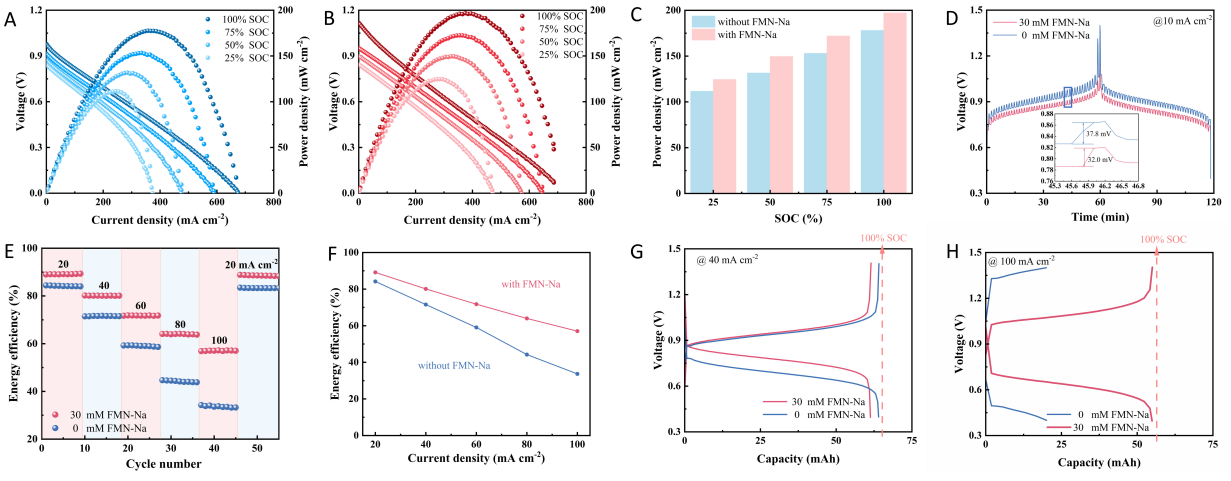

Figure 3. (A and B) Polarization curves of Fe-S RFB cells (A) without and (B) with 30.0 mM FMN-Na catalyst at various SOCs; (C) Comparison of peak power density at different SOCs; (D) GITT curves; (E) Rate performance of Fe-S RFB cells with and without 30.0 mM FMN-Na. The cell composition was 20.0 mL 2.0 M K_2S + 1.0 M KCl, with or without FMN-Na | PFSA | 25.0 mL 0.1 M $K_4[Fe(CN)_6]$ + 2.0 M KCl; (F) Comparison of average EE of Fe-S RFB cells with and without FMN-Na at different current densities; (G and H) Selected voltage-capacity profiles at current densities of (G) 40 mA cm^{-2} and (H) 100 mA cm^{-2}. FMN-Na: Flavin mononucleotide sodium salt; SOC: state of charge; Fe-S RFB: ferrocyanide-polysulfide redox flow battery; GITT: galvanostatic intermittent titration technique; PFSA: perfluorosulfonic acid membrane; EE: energy efficiency.

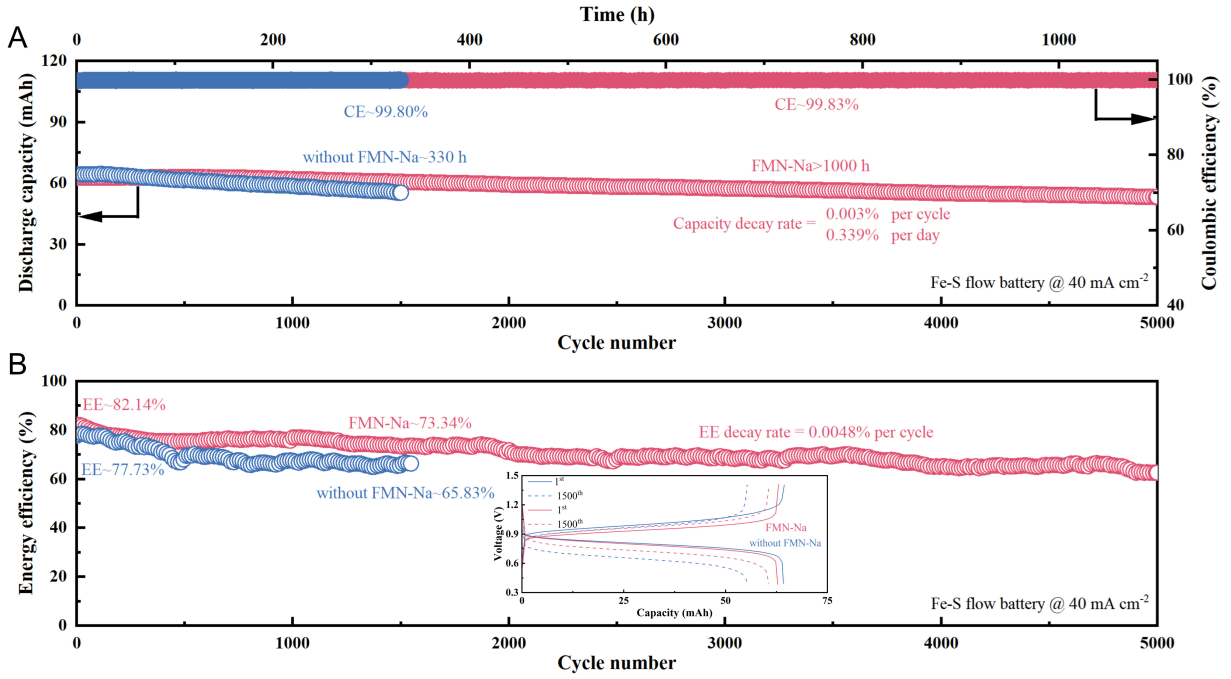

Figure 4. (A) Discharge capacity and Coulombic efficiency (CE) and (B) EE of the Fe-S RFB cells in the presence and absence of 30.0 mM FMN-Na catalyst at 40 mA cm^{-2}. The cell composition was 20.0 mL 2.0 M K_2S + 1.0 M KCl, with or without FMN-Na | PFSA | 25.0 mL 0.1 M $K_4[Fe(CN)_6]$ + 2.0 M KCl. FMN-Na: Flavin mononucleotide sodium salt; EE: energy efficiency; PFSA: perfluorosulfonic acid membrane.

FMN-Na, slightly higher than the 99.80% without FMN-Na. More importantly, FMN-Na greatly extends the cycle life: the cell with FMN-Na stably cycles for 5,000 cycles - three times longer than the catalyst-free cell (1,500 cycles). In terms of discharge capacity, FMN-Na enables a stable capacity with a decay rate of only ~0.003% per cycle or 0.339% per day.

Regarding EE [Figure 4B], the initial EE of the FMN-Na-containing cell reaches 82.14%, higher than that of the catalyst-free cell (77.73%). The FMN-Na-containing cell operates for 5,000 cycles, with an average EE decay rate of approximately 0.0048% per cycle. In contrast, the cell without FMN-Na runs for only 1,500 cycles, and its EE remains at 65.83% at the 1,500th cycle, much lower than that of the FMN-Na cell at the same cycle number (73.34%). A comparison of the 1st and 1,500th charge-discharge curves shows that the FMN-Na cell's polarization is consistently lower, consistent with previous results and further confirming the beneficial effect of FMN-Na. The gradual decline in EE is accompanied by an increasing charge-discharge voltage gap, indicating the progressive accumulation of cell polarization. After extended cycling, small amounts of sulfur deposition were observed on the carbon felt and near the sulfur-side outlet. Such deposits may remove active sulfur species from the electrolyte, cover electrochemically active sites, impede electrolyte flow, and increase cell resistance. Polysulfide crossover and the associated fouling of the membrane and electrodes may also contribute to long-term degradation. FMN-Na promotes polysulfide conversion and slows polarization buildup, but it does not completely eliminate these degradation processes.

Next, we tested the Fe-S RFB with a high-concentration catholyte where ferrocyanide was increased to 0.5 M, and FMN-Na was introduced into the anolyte. As shown in Figure 5A, the high-concentration cell with FMN-Na maintains high and stable CE during cycling, with an average CE of 99.87% and a stable cycle life of 1,000 cycles. By contrast, the cell without FMN-Na exhibits an average CE of 99.80% but lasts only 440 cycles. The advantage of FMN-Na is also evident in discharge capacity retention. The FMN-Na cell maintains a nearly stable discharge capacity over 1,000 cycles, with a capacity decay rate of 0.0043% per cycle (0.113% per

day). The catalyst-free cell suffers rapid capacity decay from the very beginning, resulting in only 440 cycles. EE comparison [Figure 5B] further confirms the positive effect of FMN-Na. The initial EE of the FMN-Na cell reaches 83.07%, much higher than the 58.89% without FMN-Na. At the 440th cycle, the FMN-Na-containing cell retained an EE of 77.34%, whereas the catalyst-free cell exhibited an EE of only 46.17% and ceased operation thereafter. The FMN-Na-containing cell continued to operate for 1,000 cycles, with its EE decreasing from 83.07% initially to 65.52%, corresponding to an average relative EE decay rate of approximately 0.021% per cycle. Charge-discharge profiles at the 1st and 400th cycles reveal that FMN-Na greatly reduces polarization and maintains superior performance. To further verify the regulatory effect of FMN-Na, we assembled an Fe-S RFB with the same high catholyte ferrocyanide concentration (0.5 M). The battery was first cycled 58 times without FMN-Na, and then 30.0 mM FMN-Na was added to the anolyte for subsequent cycling. The results show that adding FMN-Na immediately increases EE from 52.19% to 76.55% and markedly reduces polarization [Figure 5C and D]. To determine whether this KOH-free formulation using KCl as the common supporting electrolyte benefits cell performance, we assembled a more strongly alkaline control by replacing 1.0 M KCl in the anolyte with 1.0 M KOH [Supplementary Figure 4]. The catholyte continued to contain 1.0 M KCl, and all other conditions remained unchanged. Although the two cells showed similar initial EE at 40 mA cm^{-2}, the KOH/KCl cell exhibited a faster decline in EE and capacity retention, as well as substantially greater voltage drop and polarization at the 141st cycle. The difference was even more evident during extended cycling: the KOH/KCl cell was limited to approximately 150 cycles, whereas the KCl/KCl cell maintained stable operation for 1,000 cycles under the same testing conditions. These results demonstrate that avoiding externally added KOH while retaining sufficient alkalinity for FMN-Na catalysis substantially improves cell stability.

Benefiting from the accelerated polysulfide redox kinetics enabled by FMN catalysis, we further increased the effective redox-active concentration and capacity of the catholyte through redox-targeting reactions between the dissolved $[Fe(CN)_6]^{3-/4-}$ couple and PB/Prussian White (PW). In this process, PB serves as a reversible solid-state redox reservoir rather than a chemical catalyst or physical adsorption host, while the dissolved $[Fe(CN)_6]^{3-/4-}$ couple mediates charge transfer between the electrode and the PB/PW granules. The reversible and stoichiometric conversion between PB and PW therefore provides additional catholyte capacity. This mechanism was established in our previous study by CV, SOC/SOD-dependent UV–vis spectroscopy, FTIR, and XRD measurements[38]. As presented in Figure 6A, the cell was tested at 40 mA cm^{-2} with a catholyte consisting of 0.81 M $K_4[Fe(CN)_6]$ + 0.81 M $Na_4[Fe(CN)_6]$ + 0.5 M KCl (15.0 mL). After 9.0 g of PB was added at the end of the fourth cycle, the charge capacity changed only slightly from 648.9 mAh in the fourth cycle to 660.4 mAh in the fifth cycle because the freshly added PB was already in its oxidized state and therefore contributed little additional capacity during charging. During the subsequent discharge, $[Fe(CN)_6]^{3-}$ was electrochemically reduced to $[Fe(CN)_6]^{4-}$ at the electrode. The generated $[Fe(CN)_6]^{4-}$ then reduced PB to Prussian white (PW) in the catholyte reservoir and was itself oxidized back to $[Fe(CN)_6]^{3-}$, increasing the discharge capacity from 635.8 to 1,243.5 mAh. During the sixth charging process, $[Fe(CN)_6]^{3-}$ generated at the electrode oxidized PW back to PB and was reduced to $[Fe(CN)_6]^{4-}$, increasing the charge capacity to 1,261.6 mAh. This sequential capacity increase confirms the reversible participation of the PB/PW redox reservoir in charge storage. The cell remained stable in subsequent cycles. The voltage-capacity profiles [Figure 6B] clearly confirm the enhanced capacity and energy density after PB addition. The energy density increases from 36.66 Wh L^{-1} to 69.33 Wh L^{-1} based on the catholyte volume, corresponding to an effective $[Fe(CN)_6]^{3-/4-}$ concentration of 3.09 M. By further increasing the sulfide concentration in the anolyte to 8.1 M and using a high-concentration PB-containing catholyte, the cell achieved a discharge energy density of 102.12 Wh L^{-1} when normalized to the catholyte volume and 51.06 Wh L^{-1} when normalized to the combined volumes of the anolyte and catholyte [Supplementary Figure 5].

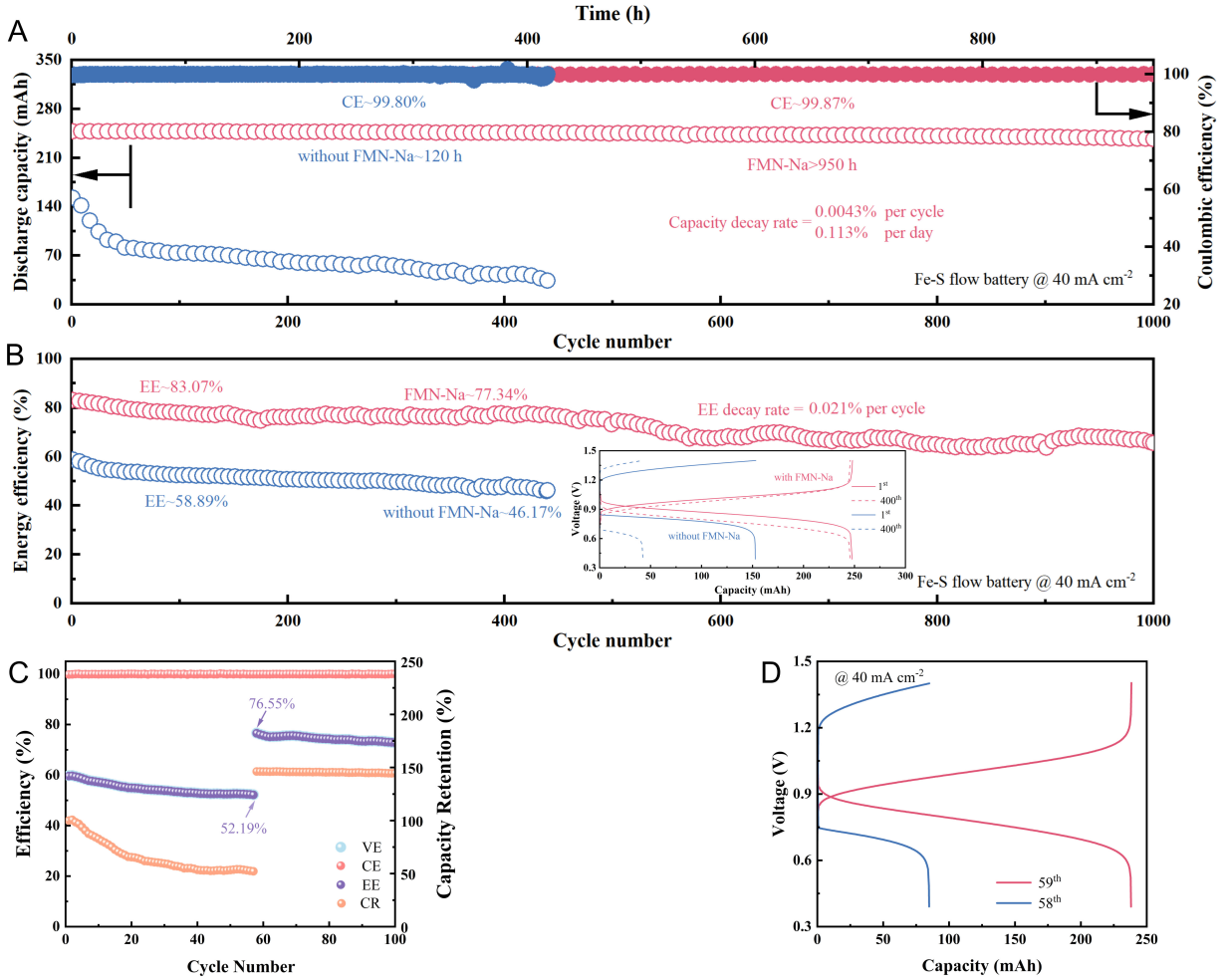

Figure 5. (A) Discharge capacity and CE curves of Fe-S RFB cells in the presence and absence of 30.0 mM FMN-Na; (B) Comparison of EE values and capacity-voltage profiles of the corresponding Fe-S RFBs. For (A) and (B), the cell composition was 40.0 mL 2.0 M K_2S + 1.0 M KCl, with or without FMN-Na | PFSA | 20.0 mL 0.25 M $K_4[Fe(CN)_6]$ + 0.25 M $Na_4[Fe(CN)_6]$ + 1.0 M KCl; (C) Cell performance of the Fe-S RFB following the midway addition of 30.0 mM FMN-Na at a current density of 40 mA cm^{-2}; (D) Corresponding voltage-capacity profiles recorded before and after FMN-Na addition. FMN-Na: Flavin mononucleotide sodium salt; CE: Coulombic efficiency; EE: energy efficiency; VE: voltage efficiency; CR: capacity retention; Fe-S RFB: ferrocyanide-polysulfide redox flow battery; PFSA: perfluorosulfonic acid membrane.

Furthermore, we successfully broadened the operating temperature range of the FMN-catalyzed Fe-S RFB to -20 to 60 °C by lowering the freezing points of electrolytes [Figure 6C]. Specifically, potassium acetate (KAc) and urea were introduced into the catholyte, and KAc alone was used in the anolyte to suppress freezing, allowing the cell to operate over a substantially broader temperature range. The freezing transition of the optimized anti-freezing catholyte was reduced to -18.9 °C. As shown in Supplementary Figure 6A, we performed ten charge-discharge cycles at -20 °C with capacities remaining around 60 mAh. The relatively large voltage gap between charge and discharge reflects the slower ion transport and redox kinetics near the freezing point. At 60 °C, the cell also retained a capacity above 60 mAh over the first ten cycles and exhibited a smaller voltage gap because of faster reaction kinetics [Supplementary Figure 6B]. However, the gradual evolution of the voltage profiles suggests greater sensitivity to electrolyte changes at elevated temperatures, where water evaporation and parasitic reactions may become increasingly significant. These results demonstrate that the cell can operate from -20 to 60 °C, although further optimization is needed for prolonged operation at the temperature limits. Notably, both the wide temperature window and ultrahigh energy density achieved in this work surpass previously reported values for Fe-S RFBs, marking a significant advancement. Based on a performance comparison with reported studies[30,32,36,39,40,43-49] [Figure 6D and

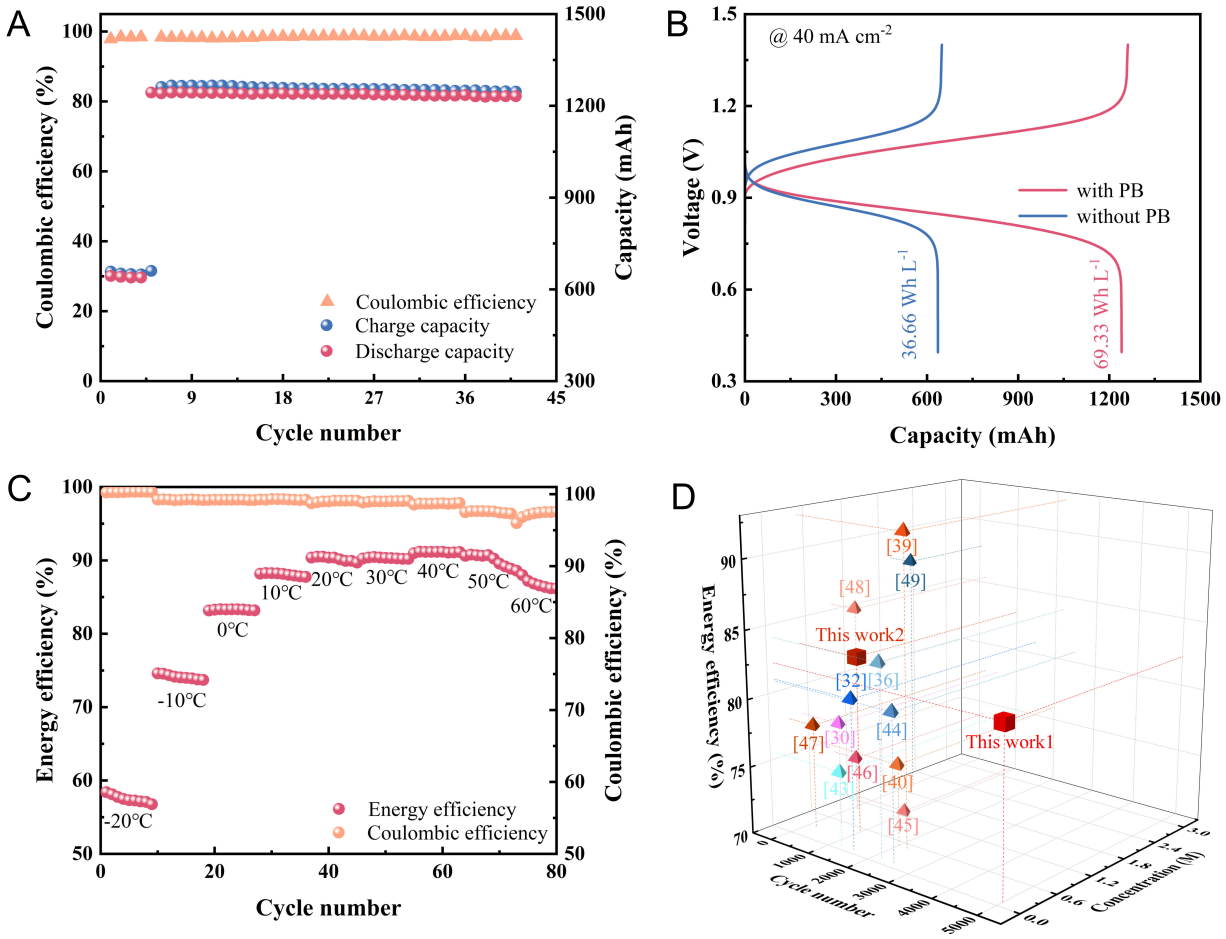

Figure 6. (A) CE and capacity curves of the Fe-S RFB cell with PB in the catholyte and FMN-Na in the anolyte; (B) Voltage-capacity curves of the Fe-S RFBs before and after PB addition; (C) Wide operating temperature range of the proposed Fe-S RFB; (D) Comprehensive performance comparison between the present Fe-S RFB and previously reported systems. Figure 6D was generated based on the data reported in references[30,32,36,39,40,43-49]. PB: Prussian blue; CE: Coulombic efficiency; Fe-S RFB: ferrocyanide-polysulfide redox flow battery; FMN-Na: flavin mononucleotide sodium salt.

Supplementary Table 4], our battery exhibits a remarkably long cycle life, high EE, and low capacity decay. Besides, the peak power density is superior to most reported neutral aqueous systems.

CONCLUSIONS

In this work, we successfully employed FMN-Na as a homogeneous catalyst in Fe-S RFBs with a KOH-free supporting electrolyte. A key distinction from previous studies is that both the catholyte and anolyte use KCl as the sole supporting electrolyte, thereby avoiding the additional OH^-/Cl^- imbalance introduced by externally added KOH and reducing changes in electrolyte composition during operation. The alkaline environment essential for FMN-Na catalysis is spontaneously generated by hydrolysis of K_2S, ensuring stable catalytic behavior while greatly simplifying electrolyte formulation and battery assembly. Considering the complex composition of polysulfide species in the anolyte and inevitable side reactions, the ferro-/ferricyanide catholyte was designed as the capacity-limiting side. Electrochemical measurements and long-term cycling tests verify that FMN-Na markedly accelerates polysulfide redox kinetics, suppresses polarization, and improves cycling stability, EE, and peak power density. The FMN-Na cell delivers stable operation for 5,000 cycles with an average CE of 99.83% and an initial EE of 82.14%, which are considerably higher than those of the catalyst-free control. Even with a high catholyte concentration of 0.5 M $[Fe(CN)_6]^{4-}$,

the modified cell retains a low capacity decay rate of 0.0043% per cycle, demonstrating reliable catalytic durability.

We further extended the operating temperature window from -20 °C to 60 °C by depressing electrolyte freezing points with KAc and urea. PB-mediated redox targeting increased the accessible ferrocyanide capacity, yielding a catholyte-volume-normalized discharge energy density of 69.33 Wh L^{-1}. Under the optimized high-concentration conditions, including an 8.1 M sulfide anolyte, this value increased to 102.12 Wh L^{-1}, corresponding to 51.06 Wh L^{-1} when normalized to the combined anolyte and catholyte volumes. Overall, this work provides a facile, low-cost, and high-performance strategy for advancing aqueous flow batteries toward practical deployment under diverse climatic conditions.

DECLARATIONS

Authors' contributions

Investigation, formal analysis, writing - original draft: Qin, C.
Formal analysis, validation, visualization: Xu, X.
Validation, discussion: Xu, Z.
Validation: Gao, C.
Investigation, discussion: Lu, B.
Conceptualization, writing - original draft, supervision: Ding, M.
Conceptualization, discussion, supervision, project administration, resources: Jia, C.

Availability of data and materials

All data and materials supporting the results of this study are included in this article and Supplementary Materials. Further data are available from the corresponding authors upon reasonable request.

AI and AI-assisted tools statement

Not applicable.

Financial support and sponsorship

This work was supported by the Key Research and Development Program of Hunan (2023SK2053) and the National Key Research and Development Program of China (2024YFE0116300).

Conflicts of interest

All authors declared that there are no conflicts of interest.

Ethical approval and consent to participate

Not applicable.

Consent for publication

Not applicable.

Supplementary Materials

Supplementary Materials

REFERENCES

1. Osman, A. I.; Chen, L.; Yang, M.; et al. Cost, environmental impact, and resilience of renewable energy under a changing climate: a review. *Environ. Chem. Lett.* **2023**, *21*, 741-64. DOI
2. Chatterjee, S.; Parsapur, R. K.; Huang, K. Limitations of ammonia as a hydrogen energy carrier for the transportation sector. *ACS. Energy. Lett.* **2021**, *6*, 4390-4. DOI

3. Ölmez, M. E.; Ari, I.; Tuzkaya, G. A simulation-based analysis of energy storage's impact on power markets for renewable energy integration. *Energy* **2025**, *326*, 136202. DOI
4. Chen, X.; Zhao, J.; Li, G.; Zhang, D.; Li, H. Recent advances in photocatalytic renewable energy production. *EM* **2022**, *2*, 200001. DOI
5. Goren, A. Y.; Dincer, I.; Khalvati, A. A comprehensive life cycle impact evaluation of hydrogen production processes for cleaner applications. *Energy* **2025**, *326*, 136182. DOI
6. Behera, P.; Sethi, N.; Dash, D. P.; Usman, M.; Sahu, P. K. Pathways to achieve carbon neutrality in emerging economies: catalyzing the role of renewable energy, green growth, ICT, and political risk. *Renew. Energy.* **2025**, *243*, 122514. DOI
7. Wei, D.; Zhang, L.; Zhang, N.; Fang, J.; Qian, Q. Optimal generation planning in a micro-grid for supplying electrical and thermal loads in order to reduce pollutant emissions. *J. Clean. Prod.* **2023**, *421*, 138531. DOI
8. Li, H.; Sun, D.; Li, B.; et al. Collaborative optimization of VRB-PS hybrid energy storage system for large-scale wind power grid integration. *Energy* **2023**, *265*, 126292. DOI
9. Rayit, N. S.; Chowdhury, J. I.; Balta-Ozkan, N. Techno-economic optimisation of battery storage for grid-level energy services using curtailed energy from wind. *J. Energy. Storage.* **2021**, *39*, 102641. DOI
10. Xie, C.; Wang, Y.; Gu, X. Synergistic integration of solid-state hydrogen storage with thermal and electrical energy storage: multi-energy collaborative optimization. *Energy. Convers. Manage.* **2025**, *343*, 120228. DOI
11. Yao, Y.; Lei, J.; Shi, Y.; Ai, F.; Lu, Y. Assessment methods and performance metrics for redox flow batteries. *Nat. Energy.* **2021**, *6*, 582-8. DOI
12. Xie, X.; Gao, J.; Wang, Z.; Li, R.; Kong, T.; Wang, Y. Challenges for aqueous organic redox flow batteries: the degradation of electrolytes and the design of ion-selective membranes. *Adv. Mater.* **2025**, e07952. DOI
13. Zhao, Z.; Liu, X.; Zhang, M.; et al. Development of flow battery technologies using the principles of sustainable chemistry. *Chem. Soc. Rev.* **2023**, *52*, 6031-74. DOI
14. Blakers, A.; Stocks, M.; Lu, B.; Cheng, C. A review of pumped hydro energy storage. *Prog. Energy.* **2021**, *3*, 022003. DOI
15. Zhang, S.; Wang, C.; Guo, Z. Batteries for grid-scale energy storage applications. *Adv. Mater.* **2025**, *37*, e16590. DOI
16. Chen, Y.; Sun, Z.; Zong, W.; Dai, Y.; Ng, K. L.; Shearing, P. R. Advanced technologies for characterizing and detecting battery thermal failure: a review. *Adv. Sci. (Weinh).* **2026**, *13*, e00050. DOI PubMed PMC
17. Zhu, F.; Guo, W.; Fu, Y. Functional materials for aqueous redox flow batteries: merits and applications. *Chem. Soc. Rev.* **2023**, *52*, 8410-46. DOI
18. Yuan, Z.; Liang, L.; Dai, Q.; et al. Low-cost hydrocarbon membrane enables commercial-scale flow batteries for long-duration energy storage. *Joule* **2022**, *6*, 884-905. DOI
19. Jang, J.; Jayasubramaniyan, S.; Lee, S. W.; Lee, H. A hexacyanomanganate negolyte for aqueous redox flow batteries. *ACS. Energy. Lett.* **2023**, *8*, 3702-9. DOI
20. He, C.; Zhang, Y.; Zhang, S.; et al. Aqueous iron-based redox flow batteries for large-scale energy storage. *Natl. Sci. Rev.* **2025**, *12*, nwaf218. DOI PubMed PMC
21. Cao, Y.; Aspuru-Guzik, A. Accelerating discovery in organic redox flow batteries. *Nat. Comput. Sci.* **2024**, *4*, 89-91. DOI PubMed
22. Wang, C.; Gao, G.; Su, Y.; et al. High-voltage and dendrite-free zinc-iodine flow battery. *Nat. Commun.* **2024**, *15*, 6234. DOI PubMed PMC
23. Edison, J. K.; Alabi, A.; Alhammadi, A.; et al. Negative electrodes in vanadium redox flow batteries: recent advances and outlook. *Adv. Appl. Energy.* **2026**, *21*, 100262. DOI
24. Hu, H.; Han, M.; Liu, J.; et al. Strategies for improving the design of porous fiber felt electrodes for all-vanadium redox flow batteries from macro and micro perspectives. *Energy. Environ. Sci.* **2025**, *18*, 3085-119. DOI
25. Yuan, T.; Chen, X.; Zhao, Y.; et al. Dual regulation of surface termination and interlayer spacing of MXene for high-performance vanadium redox flow batteries. *Chem. Eng. J.* **2026**, *533*, 174389. DOI
26. Xing, F.; Liu, T.; Yin, Y.; et al. Highly Active hollow porous carbon spheres@graphite felt composite electrode for high power density vanadium flow batteries. *Adv. Funct. Mater.* **2022**, *32*, 2111267. DOI
27. Pawar, C. M.; Madiyan, P.; Khairnar, D. D.; et al. Advances in the mixed matrix membrane for vanadium redox flow battery. *J. Energy. Storage.* **2026**, *151*, 120092. DOI
28. Yu, Z.; Jia, X.; Cai, Y.; et al. Electrolyte engineering for efficient and stable vanadium redox flow batteries. *Energy. Storage. Mater.* **2024**, *69*, 103404. DOI
29. Qi, S.; Dai, L.; Huo, W.; et al. Doping engineering strategies for electrodes and catalysts in vanadium redox flow battery. *Compos. B. Eng.* **2023**, *265*, 110947. DOI
30. Wang, F.; Luo, S.; Lei, J.; et al. Nonfluorinated membrane with a decentralized ion-transport network enables efficient and sustainable polysulfide redox flow batteries. *Sci. Adv.* **2025**, *11*, eaea0032. DOI PubMed PMC

31. Sarfaraz Khabbaz, M.; Thakur, A.; Maity, D.; et al. A polysulfide/ferricyanide redox flow battery with extended cycling. *J. Mater. Chem. A.* **2025**, *13*, 29610-20. DOI
32. Long, Y.; Xu, Z.; Wang, G.; et al. A neutral polysulfide/ferricyanide redox flow battery. *iScience* **2021**, *24*, 103157. DOI PubMed PMC
33. Liao, K.; Manthiram, A. Impact of cathode microstructure on sulfur redox kinetics in lithium-sulfur batteries. *Adv. Energy. Mater.* **2025**, *15*, 2502062. DOI
34. Pai, M. H.; Manthiram, A. Tailoring Na^+ chelation dynamics for expedient sulfur redox kinetics in low-temperature sodium-sulfur batteries. *Angew. Chem. Int. Ed. Engl.* **2025**, *64*, e202517612. DOI PubMed PMC
35. Zhou, T.; Yuan, H.; Hu, B.; et al. Boosting the electrochemical properties of polysulfide by iron(Ⅱ) phthalocyanine and its mechanism. *J. Power. Sources.* **2026**, *663*, 238936. DOI
36. Li, L.; Yan, S.; Huang, Y.; et al. Carbon felt electrode coated with WS_2 enables a high-performance polysulfide/ferricyanide flow battery. *Rare. Metals.* **2024**, *43*, 5039-47. DOI
37. Lu, G.; Zhang, J.; Wang, Z.; et al. Sulfur vacancy-rich MoS_2 anchored oxidized graphene as advanced catalysts for polysulfide-iodine redox flow battery. *Chin. Chem. Lett.* **2026**, *37*, 111650. DOI
38. Yan, S.; Huang, S.; Xu, H.; et al. Redox targeting-based neutral aqueous flow battery with high energy density and low cost. *ChemSusChem* **2023**, *16*, e202300710. DOI
39. Chen, Q.; Zhu, Y.; Zhang, S.; et al. Bislawsone as a robust redox mediator for high-performance aqueous polysulfide redox flow batteries. *Joule* **2026**, *10*, 102362. DOI
40. Lei, J.; Zhang, Y.; Yao, Y.; et al. An active and durable molecular catalyst for aqueous polysulfide-based redox flow batteries. *Nat. Energy.* **2023**, *8*, 1355-64. DOI
41. Xi, D.; Alfaraidi, A. M.; Gao, J.; et al. Mild pH-decoupling aqueous flow battery with practical pH recovery. *Nat. Energy.* **2024**, *9*, 479-90. DOI
42. Hu, M.; Wang, A. P.; Luo, J.; Wei, Q.; Liu, T. L. Cycling performance and mechanistic insights of ferricyanide electrolytes in alkaline redox flow batteries. *Adv. Energy. Mater.* **2023**, *13*, 2203762. DOI
43. Lou, X.; Fu, H.; Xu, J.; et al. Cost-effective membrane and advanced electrode for stable polysulfide-ferricyanide flow battery. *Energy. Mater. Adv.* **2022**, *2022*, 9865618. DOI
44. Liu, R.; Yan, S.; Huang, X.; et al. Metallic-phase MoS_2 nanosheets boost polysulfide redox kinetics to high-performance polysulfide-based flow batteries. *Chem. Eng. J.* **2026**, *530*, 173401. DOI
45. Zou, H.; Xu, Z.; Xiong, L.; et al. An alkaline S/Fe redox flow battery endowed with high volumetric-capacity and long cycle-life. *J. Power. Sources.* **2024**, *591*, 233856. DOI
46. Wei, X.; Xia, G.; Kirby, B.; et al. An aqueous redox flow battery based on neutral alkali metal Ferri/ferrocyanide and polysulfide electrolytes. *J. Electrochem. Soc.* **2016**, *163*, A5150-3. DOI
47. Gao, M.; Huang, S.; Zhang, F.; Lee, Y. M.; Huang, S.; Wang, Q. Successive ionic layer adsorption and reaction-deposited copper sulfide electrocatalyst for high-power polysulfide-based aqueous flow batteries. *Mater. Today. Energy.* **2020**, *18*, 100540. DOI
48. Li, W.; Qian, R.; Dong, B.; et al. Orbital hybridization-engineered electronic structure in multicomponent sulfides boosts the performance of polysulfide/iodide flow batteries. *Int. J. Miner. Metall. Mater.* **2025**, *32*, 2814-20. DOI
49. Wang, Z.; Lu, G.; Wei, T.; et al. Synergy of single atoms and sulfur vacancies for advanced polysulfide-iodide redox flow battery. *Nat. Commun.* **2025**, *16*, 2885. DOI PubMed PMC